

Variational Quantum Approximate Spectral Clustering for Binary Clustering Problems

Hyeong-Gyu Kim¹, Siheon Park², and June-Koo Kevin Rhee^{1,3,*}

¹KAIST, School of Electrical Engineering, Daejeon, 34141, South Korea

²IBM Quantum, IBM Korea Inc., Seoul, 11 07326, South Korea

³Qunova Computing, Inc., Daejeon, 34051, South Korea

*rhee.jk@kaist.edu

Abstract

In quantum machine learning, algorithms with parameterized quantum circuits (PQC) based on a hardware-efficient ansatz (HEA) offer the potential for speed-ups over traditional classical algorithms. While much attention has been devoted to supervised learning tasks, unsupervised learning using PQC remains relatively unexplored. One promising approach within quantum machine learning involves optimizing fewer parameters in PQC than in its classical counterparts, under the assumption that a sub-optimal solution exists within the Hilbert space. In this paper, we introduce the Variational Quantum Approximate Spectral Clustering (VQASC) algorithm—a NISQ-compatible method that requires optimization of fewer parameters than the system size, N , traditionally required in classical problems. We present numerical results from both synthetic and real-world datasets. Furthermore, we propose a descriptor, complemented by numerical analysis, to identify an appropriate ansatz circuit tailored for VQASC.

1 Introduction

Ever since the potential for quantum computer performance improvement on real hardware was proposed[1–3], collaborations with researchers across various fields have fostered its expansion[4, 5]. Current quantum computers face challenges with short coherence times, resulting in a limited circuit depth relative to a fully-fledged quantum computer. Despite these constraints, algorithms tailored for these specific limitations have been developed. In the current Noisy Intermediate-Scale Quantum (NISQ)[6] era, numerous algorithms have been specifically designed for noisy quantum computers. These have demonstrated performance improvements compared to classical algorithms, particularly in the fields of chemistry and mathematics[7, 8].

Quantum machine learning[9] is a notable application for NISQ devices. With the advent and continuous enhancement of quantum algorithms, a variety of quantum machine learning algorithms have been studied, showing the potential to achieve quantum advantage on NISQ devices[10, 11]. The

majority of quantum machine learning research for NISQ devices is based on the Variational Quantum Algorithm (VQA)[12] methodology. VQA uses a Parameterized Quantum Circuit (PQC)[13] to explore the Hilbert space, where the solutions to the defined problem are assumed to reside. Quantum machine learning using VQA methodology has demonstrated its ability to solve classical machine learning problems[14–16].

Various approaches have been proposed to tackle unsupervised learning tasks, each with their own strengths and weaknesses. Among the clustering algorithms, spectral clustering stands out for its capability to cluster non-convex forms. Despite its proven efficiency in clustering tasks, it is burdened with cubic time complexity, $O(N^3)$. The primary bottleneck of the spectral algorithm is the eigen-analysis of an $(N \times N)$ sparse matrix. To mitigate this high time complexity, several quantum algorithms have been proposed[17, 18], though NISQ-compatible approaches are comparatively scarce.

In this paper, we propose an approximation and implementation of the spectral clustering algorithm for NISQ devices, demonstrating its potential for performance improvement. We present a descriptor that should be considered when selecting the right ansatz for successful clustering, along with numerical results to justify our defined descriptor. By transforming the deterministic eigen-solver problem into a non-deterministic optimization problem, we aim to optimize a vector θ such that $\dim(\theta) < N$. This implies that our algorithm can identify clusters of data points by optimizing fewer parameters than the dataset’s size, N . Hence, we propose that the spectral clustering algorithm can approximately locate clusters in a dataset and can be implemented on NISQ devices, along with a method for interpreting the resultant state vector in a classical manner.

2 Results

2.1 Brief Backgrounds of Spectral Clustering

Since the introduction of the spectral clustering algorithm, it has been continuously refined and enhanced through numerous contributions across various disciplines[19–21]. Spectral clustering interprets original datasets as a graph $G = (V, E)$ and transforms them into a specific matrix called the Laplacian matrix. The unnormalized Laplacian matrix is defined as $L = D - W$, where D is a degree matrix that contains the sum of the weights of edges connected to each vertex as diagonal components, and W is an adjacency matrix that contains the weights of the edges between all node pairs in the graph G . In our setup, W contains only off-diagonal components. Although there are various methods for constructing the adjacency matrix W , in this paper, we assume that the adjacency matrix W is constructed using the Gaussian similarity function $w_{ij} = \exp(-\gamma\|\mathbf{x}_i - \mathbf{x}_j\|^2)$. We also presume that the graph G is an undirected graph, rendering both the adjacency matrix and the Laplacian matrix symmetric.

Spectral clustering can be understood in various ways, but the most popular interpretation is through the analogy of graph-cutting. Assuming a binary clustering problem, the formulation of the spectral clustering problem can be expressed as optimizing the following ratio cut[22] problem for a

given dataset:

$$\min_{A, A^c \subseteq V} \text{RatioCut}(A, A^c) \equiv \min_{A, A^c \subseteq V} \frac{\text{cut}(A, A^c)}{|A|} + \frac{\text{cut}(A, A^c)}{|A^c|} \quad (1)$$

Here, A represents a set of vertices corresponding to one clustering under consideration, while A^c denotes the set of data not contained in A . Eq. 1 can be redefined as a discrete optimization problem [21]:

$$f_i = \begin{cases} \sqrt{\frac{|A^c|}{|A|}} & \text{if } v_i \in A \\ -\sqrt{\frac{|A|}{|A^c|}} & \text{if } v_i \in A^c \end{cases} \quad (2)$$

$$\begin{aligned} \min_{\mathbf{f}} \quad & \mathbf{f}^T \mathcal{L} \mathbf{f} \\ \text{subject to} \quad & \mathbf{f} \perp \mathbf{1}, \|\mathbf{f}\| = \sqrt{N} \\ & \mathbf{f} \text{ follows the definition in Eq. 2} \end{aligned} \quad (3)$$

Here, f_i as defined in Eq. 2 represents the i -th component of vector \mathbf{f} , v_i represents the i -th vertex in the vertex set V , and \mathcal{L} stands for the Laplacian matrix. The problem specification in Eq. 3 is ideal; but since it's a discrete optimization problem, there is little chance of reaching the global minimum unless all possible permutations of A and A^c are calculated, which turns it into an NP-hard problem. The most prevalent heuristic relaxation of the discrete condition is to simply ignore discrete condition defined in Eq. 2 and turn the vector \mathbf{f} into the vector defined in continuous vector space \mathbb{R}^N .

2.2 Transition to Quantum

Eq. 3 can be converted into an optimization problem by explicitly adding the orthogonality constraint to the objective function as a penalty term, aimed at identifying a Fiedler vector corresponding to a given Laplacian matrix \mathcal{L} , can be formulated as follows:

$$\min_{\mathbf{f}} \quad \mathbf{f}^T (\mathcal{L} + \tau \cdot \mathbf{v}_0 \mathbf{v}_0^T) \mathbf{f} \quad (4)$$

$$\text{subject to} \quad F_{ii} = \begin{cases} \frac{|A^c|}{|A|} & \text{if } v_i \in A \\ \frac{|A|}{|A^c|} & \text{if } v_i \in A^c \end{cases} \quad (5)$$

$$\sum_i F_{ii} = \sqrt{N} \quad (6)$$

$$F \succeq O_N \quad (7)$$

where F denotes the outer product of the vector \mathbf{f} , τ is an arbitrarily large positive scalar, and \mathbf{v}_0 is the smallest eigenvector of the Laplacian matrix \mathcal{L} . The second term in the parenthesis is a penalty term which introduced to enforce the constraint $\mathbf{f} \perp \mathbf{1}$. Its functional role is to 'lift' the smallest eigenvector in the spectrum above the second smallest eigenvector, thereby directing the optimization process towards finding the Fiedler vector. The discrete constraint originates from

Eq. 5, which limits the components of \mathbf{f} as specified in Eq. 2. The same continuous relaxation techniques that are applicable to the classical problem can also be applied here by ignoring the discrete constraint Eq. 5.

$$\min_{\mathbf{f}} \mathbf{f}^T (\mathcal{L} + \tau \cdot \mathbf{v}_0 \mathbf{v}_0^T) \mathbf{f} \quad (8)$$

$$\text{subject to} \quad \sum_i F_{ii} = 1 \quad (9)$$

$$F \succeq O_N \quad (10)$$

Eq. 9 is a modification of Eq. 6, adapted to meet the inherent normalization constraints specific to quantum configurations. The objective function in Eq. 8 serves as the foundational framework for the following development.

Assume that the optimized vector of Eq. 8 is \mathbf{f}^* . Since the matrix in the parenthesis is a real symmetric matrix, it follows that \mathbf{f}^* is an eigenvector of the Laplacian matrix L . In the classical spectral clustering methodology, this leads to an approximation of the problem as an eigensolver problem, which involves a deterministic $O(N^3)$ eigen-decomposition. In our approach, we forgo the approximation to the eigensolver problem and instead adopt a direct continuous optimization problem setup inspired by the Ritz variational principle in quantum mechanics, a concept actively researched in the field of quantum algorithms under the name of the variational quantum eigensolver (VQE).

The classical spectral clustering algorithm assumes that the Laplacian matrix L and the vector \mathbf{f} reside in real space. In our formulation, we will extend the definition of the vector $\mathbf{f} \in \mathbb{R}^N$ to exist in complex space, $\mathbf{f} \in \mathbb{C}^N$, without loss of generality. As in typical problem setups in VQE, the vector \mathbf{f} defined in Hilbert space can be regarded as a pure quantum state and will henceforth be denoted as $|\psi(\boldsymbol{\theta})\rangle$, where $\boldsymbol{\theta}$ refers to the parameters in the PQC. The unitary operator corresponding to the PQC with parameters $\boldsymbol{\theta}$, transforming the ground state on the computational basis $|0\rangle$ into $|\psi(\boldsymbol{\theta})\rangle$, can be expressed as:

$$|\psi(\boldsymbol{\theta})\rangle = U(\boldsymbol{\theta})|0\rangle \quad (11)$$

We'll assume that the PQC operator $U(\boldsymbol{\theta})$ is a hardware-efficient ansatz (HEA) with the gate parameters $\boldsymbol{\theta}$.

In an approach directly derived from VQE methodology, the smallest eigenvalue and its corresponding eigenvector can be calculated as:

$$\langle \sigma \rangle_1 = \langle 0 | U^\dagger(\boldsymbol{\theta}) \mathcal{L} U(\boldsymbol{\theta}) | 0 \rangle \quad (12)$$

As outlined in the previous section, our interest lies in the Fiedler vector of the Laplacian matrix \mathcal{L} , corresponding to the second smallest eigenvalue and its associated eigenvector.

In VQE research field, various approaches of estimating the energy level of excited states of molecule have proposed, which is often regarded as subspace search variational quantum eigensolver (SSVQE)[23, 24]. Despite various studies have proposed, most of the algorithms are based on the ansatz that inspired from the its original problems of molecule designs, which inevitably make the

depth of the circuit longer than general ansatz usually used for quantum machine learning. Here, we detour the subspace search problem by assuming that the Laplacian matrix \mathcal{L} is not in the form of a block diagonal matrix. This implies that the associated graph G is connected, although it does not necessarily represent a complete graph.

If the Laplacian matrix is unnormalized and not in the form of a block diagonal matrix, then the smallest eigenvalue of the Laplacian matrix is 0 and its corresponding eigenvector is a constant vector. And also due to its symmetric property, all the eigenvectors are orthogonal. Hence, we can construct other formulation that shares the same ansatz and same parameters with Eq. 12 but searches the subspace that orthogonal to the smallest eigenvector.

$$\langle\sigma\rangle_2 = |\langle 0|H^{\otimes n}U(\boldsymbol{\theta})|0\rangle|^2 \quad (13)$$

Here, H stands for the Hadamard gate, and n is the log-scaled number of N which corresponds to the number of qubits in a circuit. The Eq. 13 can be implemented by using swap test [25], or more simply, appending the Hadamard gates after the ansatz circuit and get Z -expectation value of the system.

By combining Eq. 12 and Eq. 13, the following objective function can be driven:

$$J(\boldsymbol{\theta}) = \langle\sigma\rangle_1 + \tau\langle\sigma\rangle_2 \quad (14)$$

Note that Eq. 14 and Eq. 8 share the same formulation and constraints. Therefore, it is legitimate to consider that Eq. 14 has a sub-optimal solution in \mathbb{R}^N , and can be extended to \mathbb{C}^N without loss of generality. Here, τ is a positive scalar hyperparameter as defined in Eq. 8. Since the optimization algorithms rely on the history of previous objective function values or its estimations, an excessively large τ could diminish the optimizer’s efficacy in exploring the search space. Empirical analysis has shown that the second term should be initialized as closely as possible to the value of the first term. Given that $0 \leq \langle\sigma\rangle_2 \leq 1$, it is advantageous to initialize τ such that $\tau\langle\sigma\rangle_2 \approx \langle\sigma\rangle_1$, where Eq. 12 and Eq. 13 calculated from random initial parameters $\boldsymbol{\theta}_0$.

The output of classical binary spectral clustering, denoted as \mathbf{f}^* here, reveals the clustering result by the signs of the components in the vector \mathbf{f}^* . In the quantum case, however, the resultant vector is defined to reside in Hilbert space (i.e., $|\psi(\boldsymbol{\theta}^*)\rangle \in \mathbb{C}^N$), so it cannot be interpreted as simply as in the classical case. Considering the interpretation of classical spectral clustering, the optimized vector \mathbf{f}^* can be represented by mapping all the components onto a one-dimensional line. If the clustering result is ideal, two clusters are distributed on opposite sides, with zero at the center. Extending this interpretation to the complex space, each component of the optimized state vector $|\psi(\boldsymbol{\theta})\rangle$ can be plotted on the complex plane, with the two clusters distributed on different sides around the origin. Therefore, to derive clustering results from the state vector, the phase of each component must be examined.

Currently, methods for measuring the phase of each component of a state vector on a specific basis on NISQ devices are scarce. Consequently, we will estimate the signs of the components in the state vector by selecting one component and estimating its real field signs on a specific basis. This

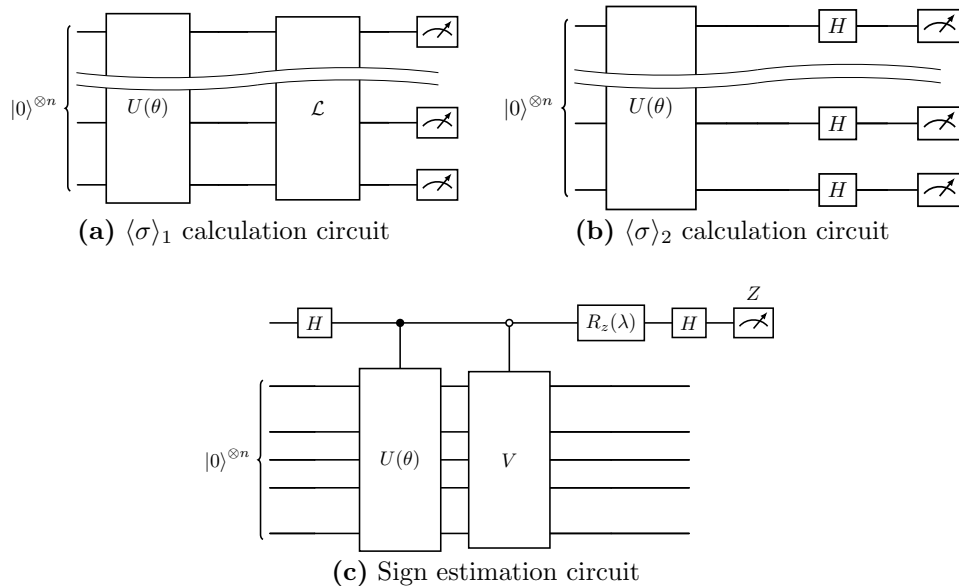


Figure 1: (a), (b) Quantum circuits for objective function calculation and (c) sign estimation circuit. The unitary block $U(\theta)$ is a HEA, while V serves as a mini-oracle unitary operator responsible for selecting one specific component from the optimized statevector. Further details can be found in the Methods section.

subroutine can be performed by iteratively running the sign estimation circuit shown in the Fig. 1-(c). One can design an orthogonal measurement basis by selecting the appropriate basis rotation angle λ . This also can be interpreted as rotating the data points on the complex plane by the angle λ . If one were to infinitely repeat this subroutine with numerous λ angles, one could determine the exact phase of the state vector components, but here only the angles $\Lambda = \{0, \frac{\pi}{4}, \frac{\pi}{2}, \frac{3\pi}{4}\}$ are sufficient, since the two-clustered data points are always distributed in a symmetric manner around the origin on the complex plane.

2.3 Phase expressibility of an Ansatz

If one can disregard issues of barren plateaus [26], it is generally advantageous to select the ansatz that demonstrates optimal *expressibility*[27]. However, our research results indicate that considering the *expressibility* of the ansatz alone does not necessarily ensure its efficacy in clustering. Thus, inspired by previous research that introduced the descriptor of *expressibility* for an ansatz, we propose a modified descriptor named *phase expressibility*.

Firstly, we assume that our interest is solely in the phases of each basis in the resultant state of an ansatz under examination. Consequently, the magnitudes of each basis will be “uniformized” to prevent them from contributing to the measurement of the *phase expressibility* of the given ansatz. The quantum states used for fidelity calculations will adhere to these same constraints; thus, the phase of each basis is the only contributing factor to the descriptor being defined.

To fulfill the assumption described above, we first consider an arbitrary pure state $|\psi_1\rangle =$

$\sum_{k=1}^{2^n} \alpha_k e^{i\phi_k} |k\rangle$. Then we postulate the existence of a tailored unitary operator T that transforms the arbitrary pure state $|\psi_1\rangle$ into the objective pure state $|\psi_2\rangle = \frac{1}{\sqrt{2^n}} \sum_k e^{i\phi_k} |k\rangle$. In the 1-qubit Bloch sphere analogy, this operation can be described as (norm-preserving) pseudo-projection of any points on the Bloch sphere onto the circumference formed by the cross-section of the Bloch sphere and the xy -plane by applying a specific unitary gate T . A brief justification for the existence of the unitary gate T is provided in the Methods section.

Since the operator T is an unitary operator, the frame potential formulation [27] for pseudo-projection of two arbitrary pure states $|\psi_\phi\rangle$ and $|\psi_\theta\rangle$ can be described without altering its fundamental expression form. This can be expressed as:

$$\mathcal{F}^{(t)} = \int_{\Phi, \Theta} |\langle \psi_\phi | T_\phi^\dagger T_\theta | \psi_\theta \rangle|^{2t} d\phi d\theta \quad (15)$$

The subscript on the unitary T indicates that it is a tailored pseudo-projection unitary for a corresponding pure state, which has the same subscript on the pure state representation. Based on the inference above, we propose the descriptor for estimating *phase expressibility*, constituting a slight modification of the original form of the *expressibility* descriptor:

$$\text{expr}_p = \text{D}_{\text{KL}}(\hat{P}_{(\text{PQC}_{\text{phase}})}(\mathbf{F}; \boldsymbol{\theta}) \| P_{(\text{Haar})}(\mathbf{F})) \quad (16)$$

Phase expressibility is inevitably related to the *expressibility* of the ansatz circuit, although the relationship is not always proportional. A more detailed explanation and various numerical examinations are provided in the Supplementary section.

Calculating Eq. 16 involves sampling the parameters $\boldsymbol{\theta}$ and the depiction of the fidelity distribution on a histogram, as performed in the original *expressibility* descriptor. This methodology inherently incurs a loss of information, a consequence of transforming the original continuous problem into a discrete estimation problem, and the constraints imposed by the number of bins in the histogram. As the number of qubits increases, fidelities from the Haar distribution tend to concentrate around 0, making it crucial to select an appropriate number of bins n_{bin} for the histogram. Unfortunately, a methodological framework to rigorously define the optimal number of bins for our setups is absent. Therefore, we empirically determined the number of bins as $n_{\text{bin}} = 150$ found to provide satisfactory accuracy for the *phase expressibility* measurement under the constraint of the number of qubits $n \leq 7$.

Algorithm 1: Variational Approximate Quantum Spectral Clustering

```
1 Input:  $(N \times N)$  Laplacian matrix  $\mathcal{L}$ , ansatz unitary  $U$ , max iteration number  $max\_itr$ ,  
   hyperparameter  $\alpha$ , measurement angles  $\mathbf{\Lambda} = \{\lambda_0, \dots, \lambda_{k-1}\}$   
2 Output: Classical resultant vector  $f^* \in \{-1, 1\}^N$   
3 Randomly initialize parameter vector  $\theta_0$  of ansatz unitary  $U$   
4  $\tau = \alpha \cdot \langle 0|U(\theta_0)^\dagger \mathcal{L}U(\theta_0)|0\rangle$   
5  $\theta = \theta_0$   
6  $itr = 0$   
7 while  $J(\theta)$  not converged or  $itr < max\_itr$  do  
8    $\langle \sigma \rangle_1 = \langle 0|U(\theta)^\dagger \mathcal{L}U(\theta)|0\rangle$   
9    $\langle \sigma \rangle_2 = |\langle 0|H^{\otimes n}U(\theta)|0\rangle|^2$   
10   $J(\theta) = \langle \sigma \rangle_1 + \tau \langle \sigma \rangle_2$   
11   $itr = itr + 1$   
12  optimize parameter vector  $\theta$  s.t.  $\min J = J(\theta)$   
13 initialize an empty list  $W$   
14 for all  $\lambda_i$  in  $\mathbf{\Lambda}$  do  
15   initialize all zero vector  $\hat{f}$  with size  $N$   
16   for all  $j$  in  $\{0, \dots, N-1\}$  do  
17      $V_j =$  corresponding  $j$ -th pauli tensor product unitary (*)  
18      $t = Re(\langle 0|V_i^\dagger e^{i\lambda_i}U(\theta^*)|0\rangle)$   
19     if  $t < 0$  then  
20        $\hat{f}_j = -1$   
21     else  
22        $\hat{f}_j = 1$   
23    $w_i = \hat{f}^T \mathcal{L} \hat{f}$   
24   append  $w_i$  into the list  $W$   
25  $opt\_idx = \text{argmin}(W)$   
26  $f^* = f_{opt\_idx}$   
27 return  $f^*$   
28 (*) Detailed instruction for constructing the unitary V in M section
```

3 Experiment

We present the performance evaluation of the variational quantum approximate spectral clustering (VQASC) algorithm. Initially, we will delineate the comparative analysis of hardware-efficient ansatz circuits and elucidate the procedure for selecting an optimal ansatz circuit. Subsequently, the chosen ansatz circuit will be applied to both synthetic datasets and real-world datasets to perform data clustering. The resulting clusters will be implemented on the IBM Q system to demonstrate the outcomes and to verify that the validation circuit is functioning properly.

It is assumed that all datasets utilized for clustering are defined within a Euclidean space, and the features of the dataset are rescaled to lie within the range of $[-1, 1]$. As previously stated, the Laplacian matrix is computed under the precondition of a connected graph, and the Gaussian similarity function is employed to measure the similarities between individual points. To sparsify the Laplacian matrix, we also employed a k -Nearest Neighbor (k -NN) graph preprocessing method. Analogous to classical spectral clustering, the correlation coefficient of the Gaussian similarity function, denoted as γ , and the parameter k in the k -NN method are important to the success of clustering. In this context, we chose an appropriate value of γ and k for each dataset.

The simulation was conducted in a noise-free environment, utilizing the *statevector* backend provided by IBM Qs open-source software for quantum computer simulations. The *L_BFGS_B*[28] optimization algorithm was selected due to its known better performance in the simulation environment[29].

3.1 Ansatz setups for experiment

To ensure the universal clustering capability of a given Laplacian matrix, both *phase expressibility* and *expressibility* must be considered. We demonstrate that *phase expressibility* and *expressibility* are closely related; however, they also evidently indicate distinct properties for a given ansatz circuit. To illustrate this observation, we consider three specific ansatz circuits.

In Figure 2, the circuit diagrams of the three ansatz circuits along with their *phase expressibility* and *expressibility* are provided. The first circuit, Circuit #A, is recognized for its favorable *expressibility* (indicated by a lower *expressibility* descriptor value) as the layers of the ansatz circuit increase. It may seem a reasonable conjecture that this would also correlate with improved performance for general clustering procedures. Contrary to this intuition, our results reveal that it possesses inferior capability for VQASC due to insufficient *phase expressibility*. The term ‘capability’ in this context refers to the convergence into the favorable local minimum and the presentation of a reasonable clustering result. Failure in this regard leads to convergence into a phenomenon called ‘settling’ where most of the statevector components have zero magnitude, except for a few components. A more detailed explanation and simulation results for the settling phenomenon can be found in the Supplementary section.

The second circuit, Circuit #B, consists solely of RY and controlled-Z operators. Because its operators are limited to varying the amplitude of qubit states initialized as the ground state $|0\rangle$ into real numbers, it exhibits very limited *expressibility*. One might conjecture that, analogous to classical spectral clustering, it could possess good clustering capability due to its confinement to

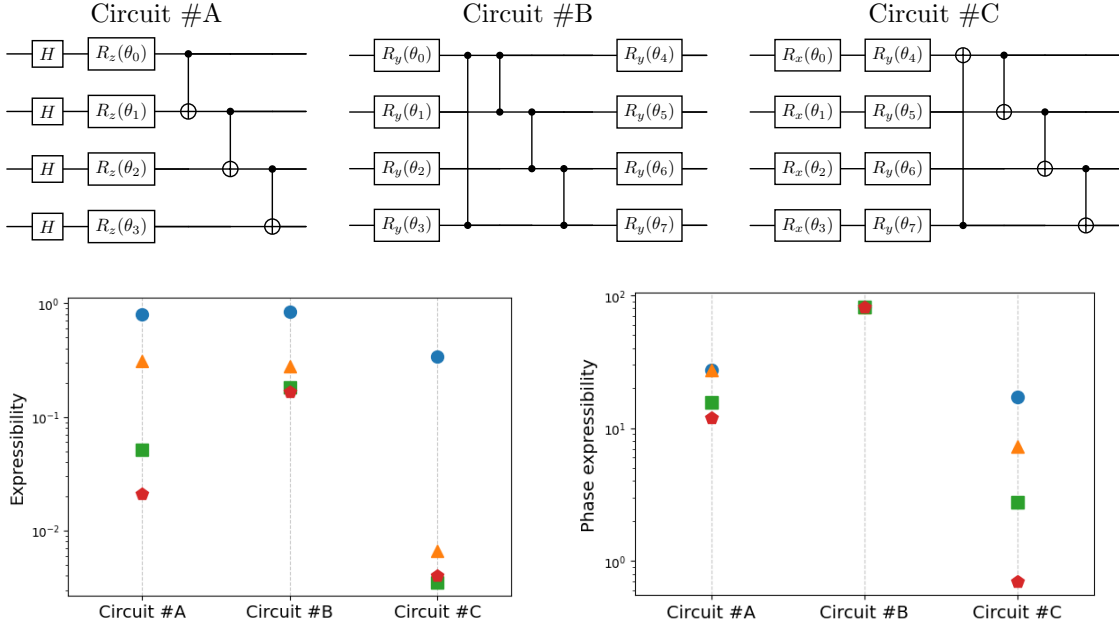


Figure 2: Circuit diagram of the three ansatz along with their *expressibility* and *phase expressibility*. The lower the expressibility, the better the state representation.

real space, which has relatively a smaller search space. However, our results indicate that it has both inferior *expressibility* and *phase expressibility*, rendering it effective only for extremely small datasets (i.e. $N \leq 8$). This finding underscores the need for the ansatz to have the ability to explore complex space to find the optimal space for minimizing the objective function, in order to achieve higher performance in clustering.

The Circuit #C shown was found to possess sufficient *phase expressibility* and *expressibility* for VQASC. It exhibits more favorable *phase expressibility* and *expressibility* compared to the other ansatz circuits. Moreover, it demonstrates a tendency towards improved *phase expressibility* and *expressibility* as the layers of the ansatz circuit increase. Therefore, our demonstration will be presented using the form of the ansatz circuit #C. This particular ansatz circuit has a linearly increasing number of parameters, specifically $2nL$, where n represents the number of qubits and L the number of layers. Further detailed reasoning is provided in the Supplementary section.

3.2 Experiment on a simulator

To evaluate the performance of the VQASC algorithm, we employ three distinct metrics. First, we use ACC (accuracy) as a direct comparison between the estimated cluster labels and the ground truth labels. Although accuracy is generally not the preferred metric for evaluating clustering performance, it is suitable in this case due to the binary nature of our clustering problem, offering an intuitive sense of performance. For a more rigorous assessment, we also utilize the Adjusted Rand Index (ARI)[30] and Normalized Mutual Information (NMI)[31] as performance metrics for clustering algorithms. Additionally, we incorporate k -NN graph preprocessing as an alternative to

constructing the Laplacian matrix, aiming to circumvent issues related to settling phenomenon. The hyperparameter τ is set to 0.8 for datasets with $N = 128$.

The VQASC algorithm was evaluated using synthetic datasets generated with the *scikit-learn* library [32]. Fig.3 showcases three such synthetic datasets. The BLOBS dataset (Fig. 3-(a),(b)) is a straightforward Gaussian distribution that serves as a foundational test for the algorithm’s basic clustering performance. The MOONS dataset (Fig. 3-(c),(d)) is employed to evaluate the algorithm’s efficacy in clustering non-convex datasets. The CIRCLES dataset (Fig. 3-(e),(f)) exemplifies extreme non-convexity in a cluster shape, making it an excellent test case for assessing clustering capabilities. We randomly created $N = 128$ data points from these synthetic datasets, using a fixed random seed, and then shuffled the dataset order. The Gaussian similarity function and the k -NN method are used for graph preprocessing. Our results, as depicted in Fig. 3, indicate high performance not only for convex-shaped clusters, as in the BLOBS dataset, but also for non-convex clusters like those in the MOONS and CIRCLES datasets. These findings confirm that VQASC is capable of handling datasets with complex distribution shapes.

The VQASC algorithm was further tested on several real-world datasets. For the IRIS dataset, which consists of 150 samples across four features, we performed no preprocessing on the high-dimensional features. To adapt the dataset for binary clustering, the ‘Iris setosa’ class was designated as one cluster, while the ‘Iris versicolor’ and ‘Iris virginica’ classes were grouped into a second cluster. In the case of the OCR dataset, which features 128×128 dimensions corresponding to handwritten digit images, we focused on the digits ‘6’ and ‘9’ to explore datasets with rotational symmetry. Owing to the high dimensionality, we reduced the OCR dataset to two features by calculating the ratios of black pixels in specific regions, using the methodology described in [33]. For the MNIST dataset, composed of 28×28 handwritten digit images, we selected only the digits ‘0’ and ‘1’ to examine the algorithm’s generalizability on larger datasets exceeding 10,000 samples. The MNIST dataset was preprocessed using Principal Component Analysis (PCA) to reduce the feature set to four dimensions. We conducted 20 trials and carefully selecting the relative factor of Gaussian similarity function and conducting k -NN graph preprocessing for each dataset, averaging the ACC, ARI, NMI metrics previously introduced. Our findings, presented in Fig.4 and Table. 1, demonstrate the algorithm’s robust performance on real-world datasets.

The ansatz circuit depicted in Fig. 5 was iterated n times, with $n = 7$ in our experiment. This allowed the algorithm to use only 98 parameters, which is less than the system size of $N = 128$, effectively reducing the optimization complexity. For real-world datasets, we randomly selected 128 samples from both the IRIS and OCR datasets. The VQASC algorithm demonstrated reliability exceeding approximately 94% on each dataset. These results indicate that VQASC can be effectively applied to real-world scenarios, provided that suitable preprocessing is conducted and that the sparse Laplacian matrix is well-defined using an appropriate metric.

3.3 Experiment on a real Hardware

For the optimized state vector $|\psi(\theta^*)\rangle$, the performance of the sign estimation circuit was validated on real IBM Q hardware, specifically the *ibmq_quito* device. Considering the constraints of long

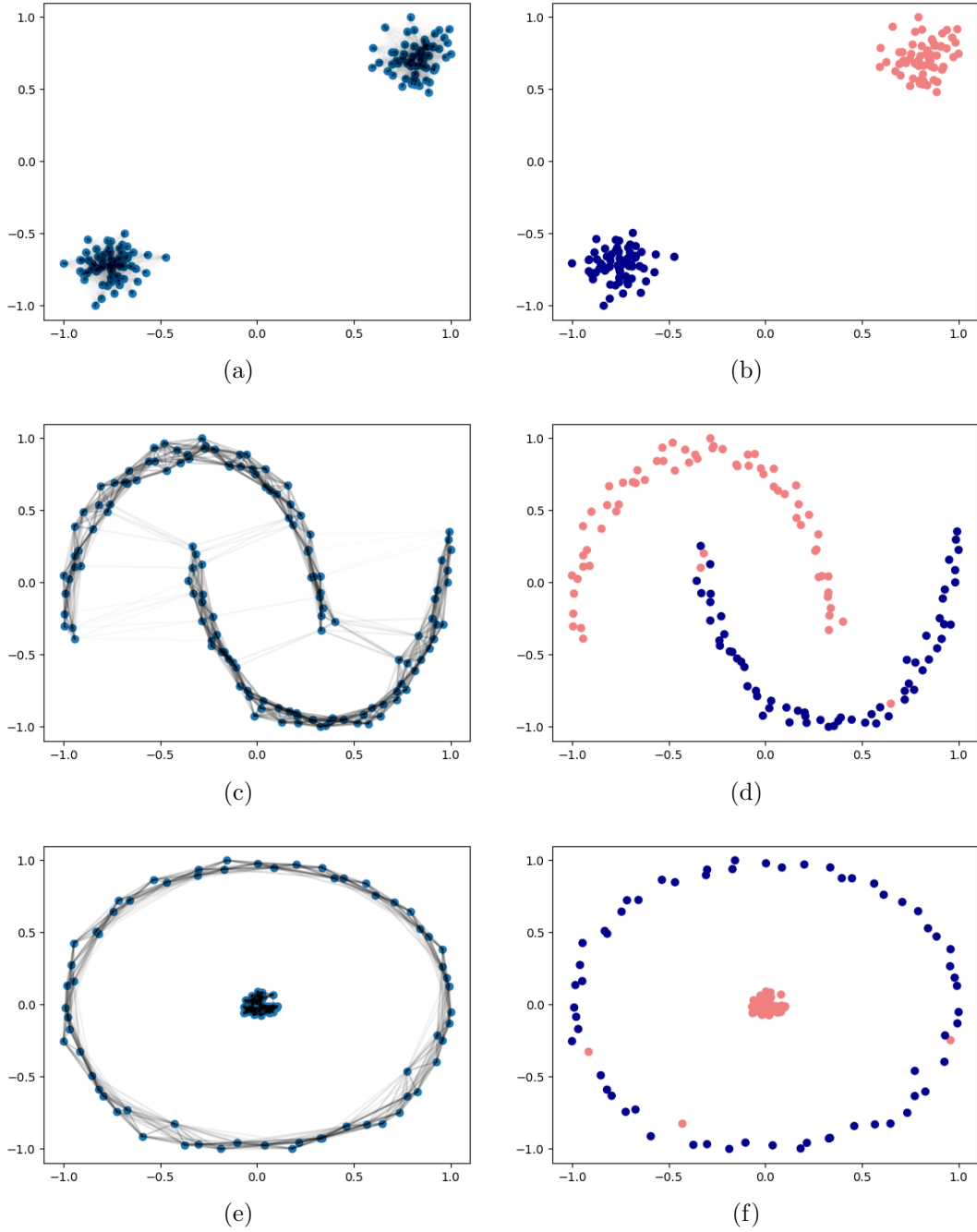


Figure 3: VQASC Results for Three Real-World Datasets: (a), (c), (e) Visualization of the Laplacian matrix for BLOBS, MOONS, and CIRCLES, and (b), (d), (f) Corresponding clustered Results.

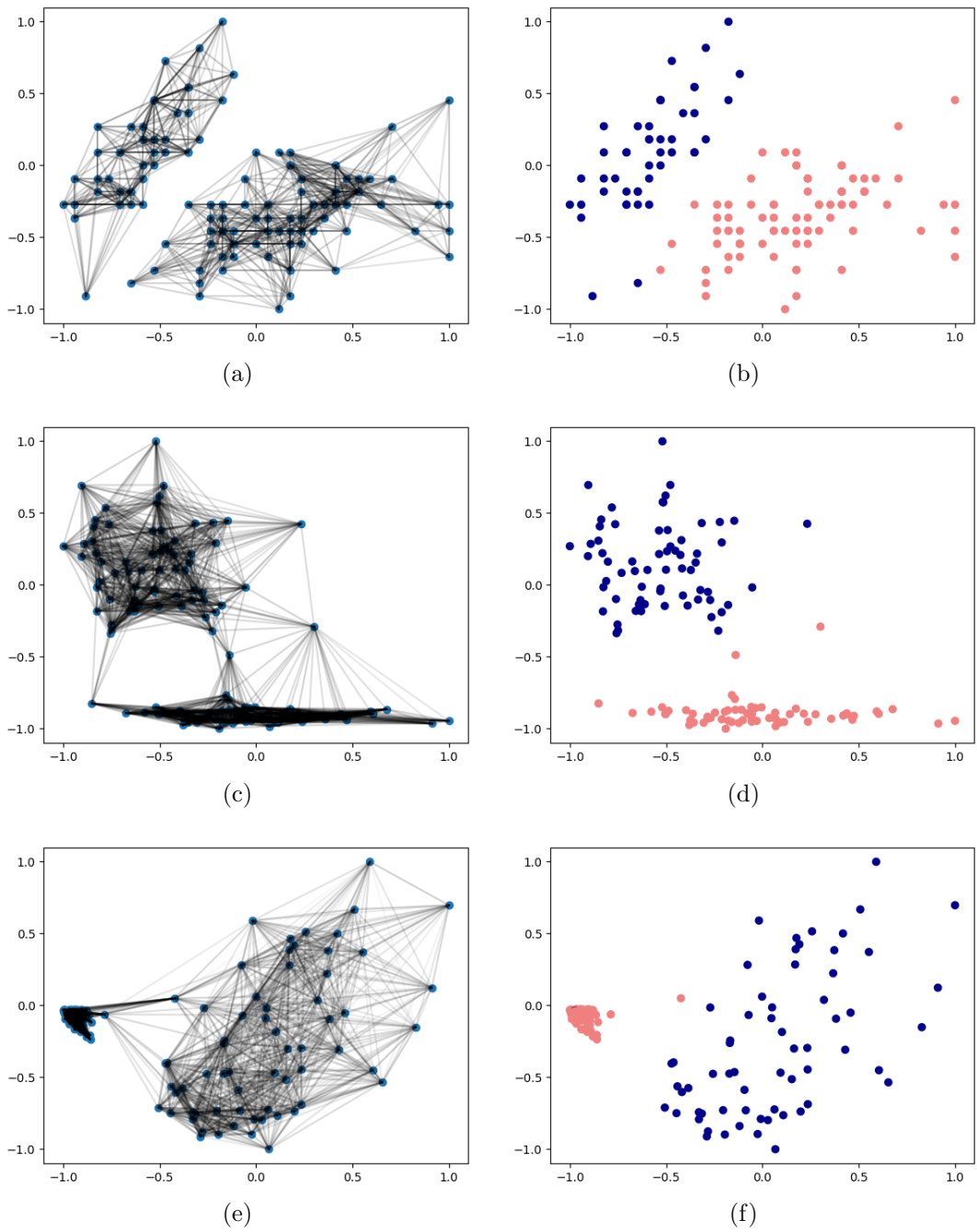


Figure 4: VQASC Results for Real-World Datasets: (a), (c), (e) Visualization of the Laplacian matrix for IRIS, OCR, and MNIST, and (b), (d), (f) corresponding clustered results. For visualization purposes, two features from high-dimensional datasets (IRIS, MNIST) are selected as axes.

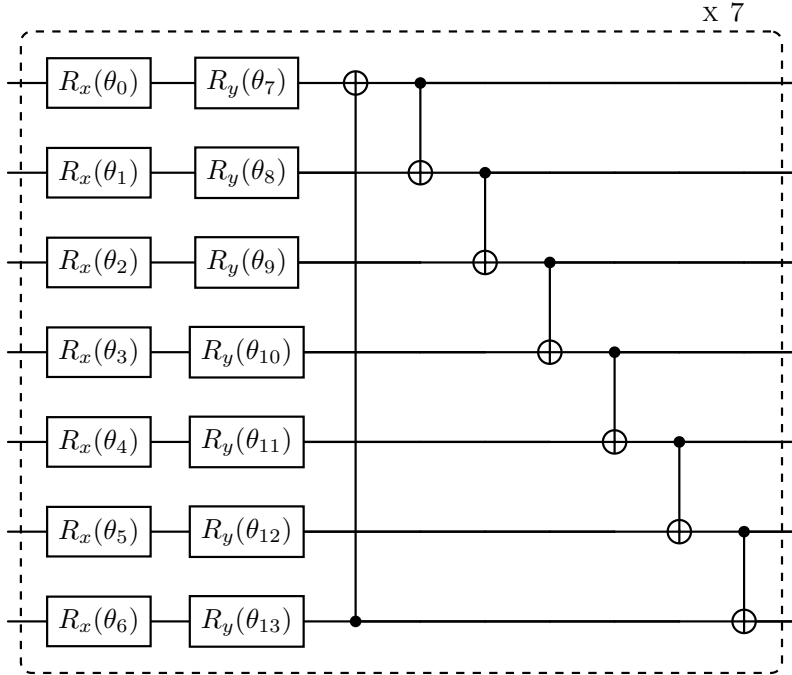
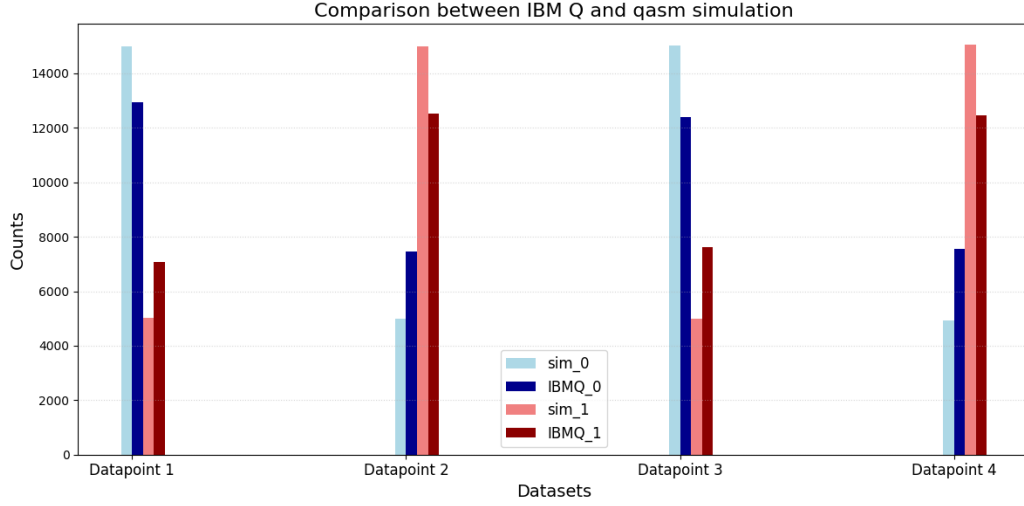


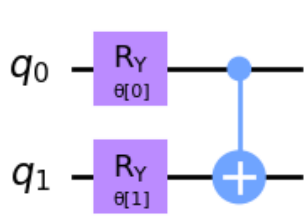
Figure 5: Ansatz circuit for simulation of synthetic and real-world datasets

Table 1: VQASC results derived from real-world datasets

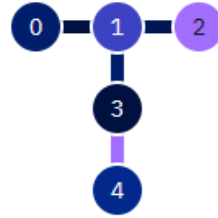
Name	N (dataset size)	features (reduced)	true labels	ACC	ARI	NMI
IRIS	128 (150)	4	{setosa, \neg setosa}	0.941	0.781	0.731
OCR	128 (200)	128×128 (2)	{‘6’, ‘9’}	0.964	0.866	0.799
MNIST	128 (14.0k)	28×28 (4)	{‘0’, ‘1’}	0.943	0.786	0.706



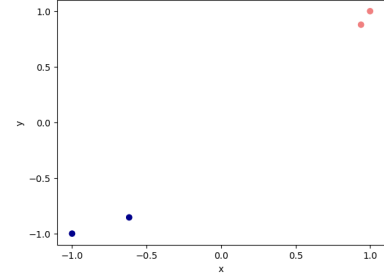
(a)



(b)



(c)



(d)

Figure 6: Sign estimation outcomes from the VQASC on a synthetic dataset, executed on IBM Q Cloud. (a) is a result of sign estimation on IBM Q cloud, (b) is an ansatz circuit used for VQASC, (c) is diagram of connectivity of *ibmq-quito*, (d) is clustered result of synthetic dataset with $N = 4$.

queue time, limited access, and small quantum volume, the experiment employed an $N = 4$ synthetic dataset, as presented in Fig. 6-(d). Additionally, the noisy environment of the *ibmq-quito* device necessitated a small ansatz circuit (Fig. 6-(b)), which has markedly low *phase expressibility* and *expressibility*. Nevertheless, empirical findings revealed that the depicted ansatz circuit is sufficient for datasets containing only $N = 4$ data points. In terms of qubit connectivity of *ibmq-quito*, the sign estimation circuit was carefully designed to minimize the number of qubit swaps by positioning the ancilla qubit as qubit 1 in Fig. 6-(c), thus ensuring connection with three adjacent qubits.

Fig. 6-(a), (d) demonstrates that the sign estimation circuit maintains its reliability despite the presence of noise and measurement errors inherent in real quantum hardware. While no error correction or mitigation methods were employed in this study due to the described limitations in accessing IBM Q hardware, it is anticipated that such errors can be minimized if known correction or mitigation techniques are implemented.

4 Discussion

In this work, a NISQ feasible quantum algorithm was presented, which provides approximated solution for spectral clustering. A classical spectral algorithm was reexamined, reconceptualizing it as a variational quantum algorithm. Instead of calculating the entire eigen-spectrum of the Laplacian matrix, the focus was on approximating the Fiedler vector with a reduced number of parameters, as compared to the original non-deterministic approach. The necessary properties for achieving accurate clustering results were also identified and numerically validated. Supporting this theory, the VQASC algorithm was tested on both synthetic and real-world datasets. It was demonstrated that, given the proper selection of an ansatz circuit, the algorithm can cluster a given dataset with high accuracy.

The numerical results proposed provide evidence that the VQASC algorithm can approximate the deterministic $O(N^3)$ algorithm, transforming it into a non-deterministic optimization algorithm that optimizes $\dim(\boldsymbol{\theta}) \leq N$ parameters. Furthermore, the space complexity of the algorithm may be reduced from $O(N)$ to $O(\log N)$ due to the encoding and processing of the dataset in qubit form. Despite these relaxations and advantages, it is not claimed that the VQASC algorithm necessarily improves upon the performance of the original deterministic eigensolver problem. Inherent challenges in the quantum-classical hybrid optimization structure due to non-convex landscape of cost function complicate the precise calculation of time complexity. Future studies may investigate the application of the parameter-shift rule[34] and the analytical approach to time complexity in gradient descent within this context, given certain error bounds.

This study also explored the application of the variational quantum algorithm methodology in clustering, highlighting the particular importance of the *phase expressibility* descriptor—a related but distinct concept. Since the algorithm encodes the Fiedler vector value into the ansatz circuit, it is anticipated that the concept of *phase expressibility* could be linked to the encoding of classical data, offering valuable insights for future research. However, analyzing the ansatz circuit as a phase encoder presents challenges due to the complexity of the inherent mathematical description of the quantum circuit, which currently precludes an analytical approach. Furthermore, since the *expressibility* of a circuit does not necessarily improve with an increase in the number of layers or changes in the entanglement structure, *phase expressibility* may resist generalization. While extensive efforts were made to identify the most favorable ansatz circuit through numerical considerations across various circuits, it is believed that a more efficient ansatz circuit for clustering may still be discovered.

On the other hand, the challenge of efficiently encoding input data persists within our algorithm. As the methodology inspired concepts from the VQE, we interpret the Laplacian matrix as a Hamiltonian matrix and optimize the ansatz circuit to acquire its first excited state—the Fiedler vector, in our approach. However, an efficient means of representing the Laplacian matrix as a unitary operator remains elusive. The most general method of expressing the Laplacian matrix as a unitary matrix involves decomposing it as a tensor product of Pauli operators. However, this approach triggers an exponential growth in computation, as the permutations of Pauli operators increase with the number of qubits. Thus, a more sophisticated method of data encoding is requisite for achieving

a significant improvement in time complexity.

The VQASC algorithm presumes that the Laplacian matrix corresponds to an unnormalized, connected graph. In the classical spectral clustering algorithm community, however, there exist numerous variants of spectral clustering methodologies. Some of these are known to impose different constraints and have been found to yield better performance compared to the results under the constraints we implemented. Such approaches could be utilized if a method for finding multiple eigenstates for the Laplacian matrix were discovered. This approach could be more favorable considering the inherent convexity of the Laplacian matrix owing to its positive semi-definite property. We believe that spectral clustering can be articulated in a more concise and refined form. While the objective function we proposed is intuitive and directly derived from the original spectral clustering problem, offering little room for error, it inherits constraints from that original problem - namely, the expression of clustering information through the signs of the Fiedler vector. Therefore, VQASC requires a highly expressive ansatz circuit to ensure accurate clustering. This necessity may not only raise the settling issue as described in the Supplementary section, but also prove critical, as high *expressibility* can lead to the barren plateaus problem[26]. If the problem setup were altered to optimize magnitude without considering phase—instead of expressing all possible phases—we conjecture that the *expressibility* constraints for VQASC would be relaxed, thereby reducing the likelihood of encountering the settling and barren plateaus. The adaptability of such variant spectral clustering algorithms to variational quantum algorithms remains an intriguing subject for future research.

5 Methods

5.1 Sign estimation circuit

The sign estimation circuit depicted in Fig. 1-(c), modified from the original hadamard test[35], has been adapted in this study to serve our sign estimation purposes. Composed of two conditional unitary blocks, this circuit incorporates an unitary block U that corresponds to the ansatz circuit unitary articulated in Eq. 11 with optimized parameters θ^* . A second unitary block V is defined as

$$V = \bigotimes_{i=1}^n \sigma_i^s, \quad \sigma_i^s \in \{I, X\}, \quad (17)$$

for an n -qubit circuit. V operates as a mini-oracle circuit, selecting a single component of the state vector $|\psi^*\rangle = U(\theta^*)|0\rangle$. The unitary block V is essentially a tensor product of I and X operators of the Pauli operators. Based on the encoding scheme employed (in our case, little-endian, zero-indexed), one can isolate a single component from the state vector by selecting the corresponding permutation of the Pauli operators in a binary manner. For instance, in a 2-qubit circuit, constructing $V = I \otimes X$ leaves the first component ($= 01_{(2)}$) of $|\psi\rangle$ unaffected while nullifying the magnitude of all other components. Conversely, $V = X \otimes I$ will retain the second component ($= 10_{(2)}$) of $|\psi\rangle$ and reduce the magnitude of all other components to zero.

Referencing Figure 3, the quantum state prior to measurement of the ancilla qubit can be expressed as follows:

$$|\phi_1\rangle = \frac{1}{2}[e^{-i\frac{\lambda}{2}}(I \otimes V)(|00\rangle + |10\rangle) + e^{i\frac{\lambda}{2}}(I \otimes U)(|00\rangle - |10\rangle)], \quad (18)$$

$$\begin{aligned} \rho_1 &= |\phi_1\rangle\langle\phi_1| \\ &= \frac{1}{4}[(I \otimes V)(|00\rangle + |10\rangle)(\langle 00| + \langle 10|)(I \otimes V^\dagger) \\ &\quad + (I \otimes U)(|00\rangle - |10\rangle)(\langle 00| - \langle 10|)(I \otimes U^\dagger) \\ &\quad + e^{i\lambda}(I \otimes U)(|00\rangle - |10\rangle)(\langle 00| + \langle 10|)(I \otimes V^\dagger) \\ &\quad + e^{-i\lambda}(I \otimes V)(|00\rangle + |10\rangle)(\langle 00| - \langle 10|)(I \otimes U^\dagger)]. \end{aligned} \quad (19)$$

The probability of measuring ‘0’ for the ancilla qubit is articulated as follows:

$$\begin{aligned} &\text{tr}(\rho_1(|0\rangle\langle 0| \otimes \sum_{k=0}^{2^n-1} |k\rangle\langle k|)) \\ &= \frac{1}{4} \sum_{k=0}^{2^n-1} [\langle 0k|(I \otimes V)(|00\rangle + |10\rangle)(\langle 00| + \langle 10|)(I \otimes V^\dagger)|0k\rangle \\ &\quad + \langle 0k|(I \otimes U)(|00\rangle - |10\rangle)(\langle 00| - \langle 10|)(I \otimes U^\dagger)|0k\rangle \\ &\quad + e^{i\lambda}(\langle 0k|(I \otimes U)(|00\rangle - |10\rangle)(\langle 00| + \langle 10|)(I \otimes V^\dagger)|0k\rangle) \\ &\quad + e^{-i\lambda}(\langle 0k|(I \otimes V)(|00\rangle + |10\rangle)(\langle 00| - \langle 10|)(I \otimes U^\dagger)|0k\rangle)] \\ &= \frac{1}{4}[2 + e^{i\lambda} \sum_{k=0}^{2^n-1} \langle k|U|0\rangle\langle 0|V^\dagger|k\rangle + e^{-i\lambda} \sum_{k=0}^{2^n-1} \langle k|V|0\rangle\langle 0|U^\dagger|k\rangle] \\ &= \frac{1}{4}[2 + e^{i\lambda} \sum_{k=0}^{2^n-1} \langle 0|V^\dagger|k\rangle\langle k|U|0\rangle + e^{-i\lambda} \sum_{k=0}^{2^n-1} \langle 0|U^\dagger|k\rangle\langle k|V|0\rangle] \\ &= \frac{1}{4}[2 + e^{i\lambda}\langle 0|V^\dagger U|0\rangle + e^{-i\lambda}\langle 0|U^\dagger V|0\rangle] \\ &= \frac{1}{4}[2 + \langle 0|V^\dagger e^{i\lambda} U|0\rangle + \langle 0|U^\dagger e^{-i\lambda} V|0\rangle] \\ &= \frac{1}{4}[2 + 2\text{Re}\langle 0|V^\dagger e^{i\lambda} U|0\rangle] \end{aligned} \quad (20)$$

By employing similar derivation, the probability of measuring ‘1’ for the ancilla qubit can be deduced as follows:

$$\text{tr}(\rho_1(|1\rangle\langle 1| \otimes \sum_{k=0}^{2^n-1} |k\rangle\langle k|)) = \frac{1}{4}[2 - 2\text{Re}\langle 0|V^\dagger e^{i\lambda} U|0\rangle] \quad (21)$$

Consequently, the Z -expectation value of the ancilla qubit is given by $\langle \sigma^z \rangle_a = \text{Re}\langle 0|V^\dagger e^{i\lambda} U|0\rangle$. Therefore, by calculating $\langle \sigma^z \rangle_a$, one can deduce the sign of one component in the state vector for

a given phase λ . By iterating the sign estimation circuit N times with possible permutations of V , one can ascertain the estimated sign of the state vector $|\psi^*\rangle$.

5.2 The existence of arbitrary pseudo-projection unitary T

Given two arbitrary pure states $|\psi_1\rangle$ and $|\psi_2\rangle$, it is possible to define a unitary operator T as follows:

$$T = |\psi_2\rangle\langle\psi_1| + |\psi_2^\perp\rangle\langle\psi_1^\perp|, \quad (22)$$

$$T^\dagger = |\psi_1\rangle\langle\psi_2| + |\psi_1^\perp\rangle\langle\psi_2^\perp|. \quad (23)$$

Upon applying the unitary operator T to $|\psi_1\rangle$, the resultant state is $|\psi_2\rangle$:

$$T|\psi_1\rangle = |\psi_2\rangle\langle\psi_1|\psi_1\rangle + |\psi_2^\perp\rangle\langle\psi_1^\perp|\psi_1\rangle = |\psi_2\rangle. \quad (24)$$

Obviously, the unitary operator T satisfies the defining property of all unitary operators, namely $TT^\dagger = T^\dagger T = I$. This suggests the existence of a unitary operator capable of facilitating a transformation between any two arbitrary pure states. If $|\psi_1\rangle$ and $|\psi_2\rangle$ are defined as follows, the existence of the so-called pseudo-projection unitary operator T can be validated:

$$|\psi_1\rangle = \sum_{k=1}^{2^n} \alpha_k e^{i\phi_k} |k\rangle, \quad (25)$$

$$|\psi_2\rangle = \frac{1}{\sqrt{2^n}} \sum_{k=1}^{2^n} e^{i\phi_k} |k\rangle. \quad (26)$$

where α_k denotes the amplitude of the basis, adhering to the condition $\sum_{k=1}^{2^n} \alpha_k^2 = 1$.

Acknowledgments

This work was supported by Samsung Research Funding & Incubation Center of Samsung Electronics under Project Number SRFC-TF2003-01. We acknowledge use of IBM Q for this work. The views expressed are those of the authors and do not reflect the official policy or position of IBM or the IBM Q team.

References

1. Arute F, Arya K, Babbush R, et al. Quantum Supremacy using a Programmable Superconducting Processor. *Nature* 2019;574:505–10.
2. Wu Y, Bao WS, Cao S, et al. Strong Quantum Computational Advantage Using a Superconducting Quantum Processor. *Phys. Rev. Lett.* 18 2021;127:180501.

3. Madsen LS, Laudenbach F, Askarani MF, et al. Quantum computational advantage with a programmable photonic processor. *Nature* 2022;606:75–81.
4. Quantum GA, Collaborators*†, Arute F, et al. Hartree-Fock on a superconducting qubit quantum computer. *Science* 2020;369:1084–9.
5. Bravo-Prieto C, LaRose R, Cerezo M, Subasi Y, Cincio L, and Coles PJ. Variational Quantum Linear Solver. 2020. arXiv: 1909.05820 [quant-ph].
6. Preskill J. Quantum computing in the NISQ era and beyond. *Quantum* 2018;2:79.
7. Farhi E, Goldstone J, and Gutmann S. A Quantum Approximate Optimization Algorithm. 2014. arXiv: 1411.4028 [quant-ph].
8. Huang HY, Bharti K, and Reberntrost P. Near-term quantum algorithms for linear systems of equations. 2019. arXiv: 1909.07344 [quant-ph].
9. Biamonte J, Wittek P, Pancotti N, Reberntrost P, Wiebe N, and Lloyd S. Quantum machine learning. *Nature* 2017;549:195–202.
10. Havlíček V, Córcoles AD, Temme K, et al. Supervised learning with quantum-enhanced feature spaces. *Nature* 2019;567:209–12.
11. Schuld M and Killoran N. Quantum machine learning in feature Hilbert spaces. *Physical review letters* 2019;122:040504.
12. Cerezo M, Arrasmith A, Babbush R, et al. Variational quantum algorithms. *Nature Reviews Physics* 2021;3:625–44.
13. Benedetti M, Lloyd E, Sack S, and Fiorentini M. Parameterized quantum circuits as machine learning models. *Quantum Science and Technology* 2019;4:043001.
14. Otterbach JS, Manenti R, Alidoust N, et al. Unsupervised Machine Learning on a Hybrid Quantum Computer. 2017. arXiv: 1712.05771 [quant-ph].
15. Jerbi S, Gyurik C, Marshall S, Briegel H, and Dunjko V. Parametrized Quantum Policies for Reinforcement Learning. In: *Advances in Neural Information Processing Systems*. Ed. by Ranzato M, Beygelzimer A, Dauphin Y, Liang P, and Vaughan JW. Vol. 34. Curran Associates, Inc., 2021:28362–75. URL: https://proceedings.neurips.cc/paper_files/paper/2021/file/eec96a7f788e88184c0e713456026f3f-Paper.pdf.
16. Park S, Park DK, and Rhee JKK. Variational quantum approximate support vector machine with inference transfer. *Scientific Reports* 2023;13:3288.
17. Kerenidis I and Landman J. Quantum spectral clustering. *Physical Review A* 2021;103:042415.
18. Volya D and Mishra P. Quantum Spectral Clustering of Mixed Graphs. In: *2021 58th ACM/IEEE Design Automation Conference (DAC)*. 2021:463–8. DOI: 10.1109/DAC18074.2021.9586308.
19. Shi J and Malik J. Normalized cuts and image segmentation. *IEEE Transactions on pattern analysis and machine intelligence* 2000;22:888–905.
20. Ng A, Jordan M, and Weiss Y. On spectral clustering: Analysis and an algorithm. *Advances in neural information processing systems* 2001;14.

21. Luxburg U von. A Tutorial on Spectral Clustering. 2007. arXiv: 0711.0189 [cs.DS].
22. Hagen L and Kahng AB. New spectral methods for ratio cut partitioning and clustering. *IEEE transactions on computer-aided design of integrated circuits and systems* 1992;11:1074–85.
23. Nakanishi KM, Mitarai K, and Fujii K. Subspace-search variational quantum eigensolver for excited states. *Physical Review Research* 2019;1:033062.
24. Kirby WM, Tranter A, and Love PJ. Contextual subspace variational quantum eigensolver. *Quantum* 2021;5:456.
25. Buhrman H, Cleve R, Watrous J, and Wolf R de. Quantum Fingerprinting. *Phys. Rev. Lett.* 16 2001;87:167902.
26. McClean JR, Boixo S, Smelyanskiy VN, Babbush R, and Neven H. Barren plateaus in quantum neural network training landscapes. *Nature communications* 2018;9:4812.
27. Sim S, Johnson PD, and Aspuru-Guzik A. Expressibility and entangling capability of parameterized quantum circuits for hybrid quantum-classical algorithms. *Advanced Quantum Technologies* 2019;2:1900070.
28. Byrd RH, Lu P, Nocedal J, and Zhu C. A limited memory algorithm for bound constrained optimization. *SIAM Journal on scientific computing* 1995;16:1190–208.
29. Pellow-Jarman A, Sinayskiy I, Pillay A, and Petruccione F. A comparison of various classical optimizers for a variational quantum linear solver. *Quantum Information Processing* 2021;20:202.
30. Hubert L and Arabie P. Comparing partitions. *Journal of classification* 1985;2:193–218.
31. Lancichinetti A, Fortunato S, and Kertész J. Detecting the overlapping and hierarchical community structure in complex networks. *New journal of physics* 2009;11:033015.
32. Pedregosa F, Varoquaux G, Gramfort A, et al. Scikit-learn: Machine learning in Python. *Journal of machine learning research* 2011;12:2825–30.
33. Li Z, Liu X, Xu N, and Du J. Experimental realization of a quantum support vector machine. *Physical review letters* 2015;114:140504.
34. Schuld M, Bergholm V, Gogolin C, Izaac J, and Killoran N. Evaluating analytic gradients on quantum hardware. *Physical Review A* 2019;99:032331.
35. Aharonov D, Jones V, and Landau Z. A polynomial quantum algorithm for approximating the Jones polynomial. In: *Proceedings of the thirty-eighth annual ACM symposium on Theory of computing.* 2006:427–36.

6 Supplementary

6.1 Settling Behavior during the Optimization Process

Not only *expressibility* itself but also the *phase expressibility* of an ansatz circuit for VQASC is important for the performance of the clustering. These two descriptors are not proportional, and a deficiency in either could result in a failed clustering process. A notable challenge in VQASC is the phenomenon of “settling”, an unintended behavior that manifests during the optimization process. This issue arises from the limited *expressibility* of the ansatz circuit, particularly in its ability to capture the phase variations for each basis state in $|\psi(\boldsymbol{\theta})\rangle$. In classical settings, \mathbf{f} can be optimized to its global minimum due to its complete freedom to alter its components in the vector and semidefinite-programming(SDP) problem setups in Eq. 8. However, when \mathbf{f} is extended to complex space and expressed through HEA circuits, $|\psi(\boldsymbol{\theta})\rangle$, the *phase expressibility* becomes a critical factor for successful optimization. Insufficient *phase expressibility* may lead to the optimizer ‘settling’ instead of a sub-optimal solution, reducing the magnitudes to zero for most components.

Fig. S1 highlights the importance of *phase expressibility*. For setups with $n = 7$, both Circuit #2 and Circuit #9 exhibit similar expressibility; however, Circuit #2 demonstrates favorable *phase expressibility*. Consequently, the clustering results using Circuit #2, as shown in Fig. S1-(a), are more satisfactory compared to those using Circuit #9, depicted in Fig. S1-(c). This difference becomes more apparent upon examining the optimized state vector $|\psi^*\rangle$ plotted on the complex plane, as shown in Fig. S1-(b) and (d). Fig. S1-(b) reveals a clearer and more distinguishable cluster around the origin in the complex plane, while Fig. S1-(d) indicates that most data points are concentrated at the origin. The latter can be interpreted as the algorithm settling for the unfavorable solution due to lack of *phase expressibility*.

Moreover, if clustering occurs under the constraints of a connected graph with a Gaussian similarity function, the precise selection of the correlation parameter γ also becomes crucial. With high γ , the entries of the Laplacian matrix become exponentially low, which consequently necessitates a high magnitude for all components of $|\psi^*\rangle$. This is conjectured to be generally unfeasible for HEA circuits, as they express the magnitudes and phases only through the multiplication of trigonometric functions. Hence, for successful clustering, both *expressibility* and *phase expressibility* must be considered.

We conjecture that optimizing the ansatz circuit parameters to express all possible phases for each component may not be the most effective strategy for representing the clustering result. We suggest that it may be possible to modify the objective function to optimize the magnitudes of the quantum state instead of the phases. This approach appears more logical, as the observation of the settling phenomenon for VQASC paradoxically shows that, for HEA circuits, it is easier to express zero magnitudes than to express all possible phases while maintaining non-zero magnitudes. Although this approach necessitates subspace search for estimating multiple eigenstates, we conjecture that the number of parameters to be optimized can still be reduced to less than N due to anticipated relaxation of the *expressibility* requirements for the ansatz circuit. We will leave this research topic for future study.

6.2 Comparison of Ansatz Circuits in Terms of expressibility and phase expressibility

Initially, we examined the *expressibility* and *phase expressibility* of circuits delineated in a preceding research paper[27], upholding the same constraints with $n = 4$. From the perspective of *phase expressibility*, the circuits wherein *phase expressibility* escalates with an increase in the number of layers include #2, #11, #7, #8, #12, #6, #5. However, in the context of our work, which focuses on utilizing fewer parameters for the optimization of the Fiedler vector \mathbf{f}^* , circuits #5 and #6 are excluded due to an exponential increase in the number of parameters, specifically $(n^2 + 3n)L$.

While circuits #11 and #12 also witness a linear increase in the number of parameters, it is significant to note that this increase $(4n-4)L$ can substantiate their clustering capabilities when $N > 2^8$. This is a critical threshold beyond which the barren plateaus phenomena is easily confronted. Similarly, circuits #7 and #8 are excluded due to the increase in the number of parameters $(5n-1)L$. Thus, we utilized circuit #2 for testing, given that the number of parameters is $2nL$.

Furthermore, we conducted additional estimates of *expressibility* and *phase expressibility* for circuit #2, incorporating different combinations of rotation gates, entanglement gates, and entanglement types. The results revealed that under the constraint of $n = 7$, circuit #23 exhibited the most favorable outcome for our purpose. Consequently, we employed circuit #23 for the $N = 128$ dataset.

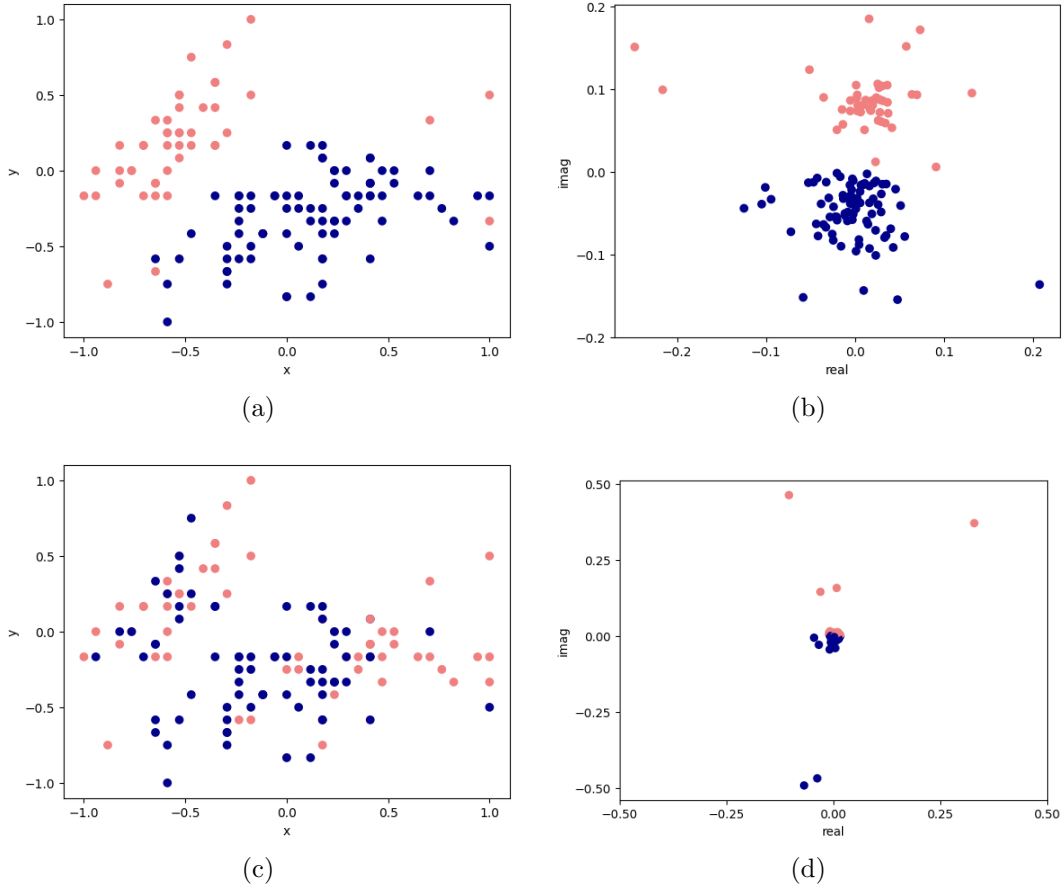


Figure S1: Clustering results for the IRIS dataset with sample size $N = 128$: (a), (b) Clustering outcome and the complex plot of the resulting vector using Circuit #2; (c), (d) Clustering outcome and the complex plot of the resulting vector using Circuit #9.

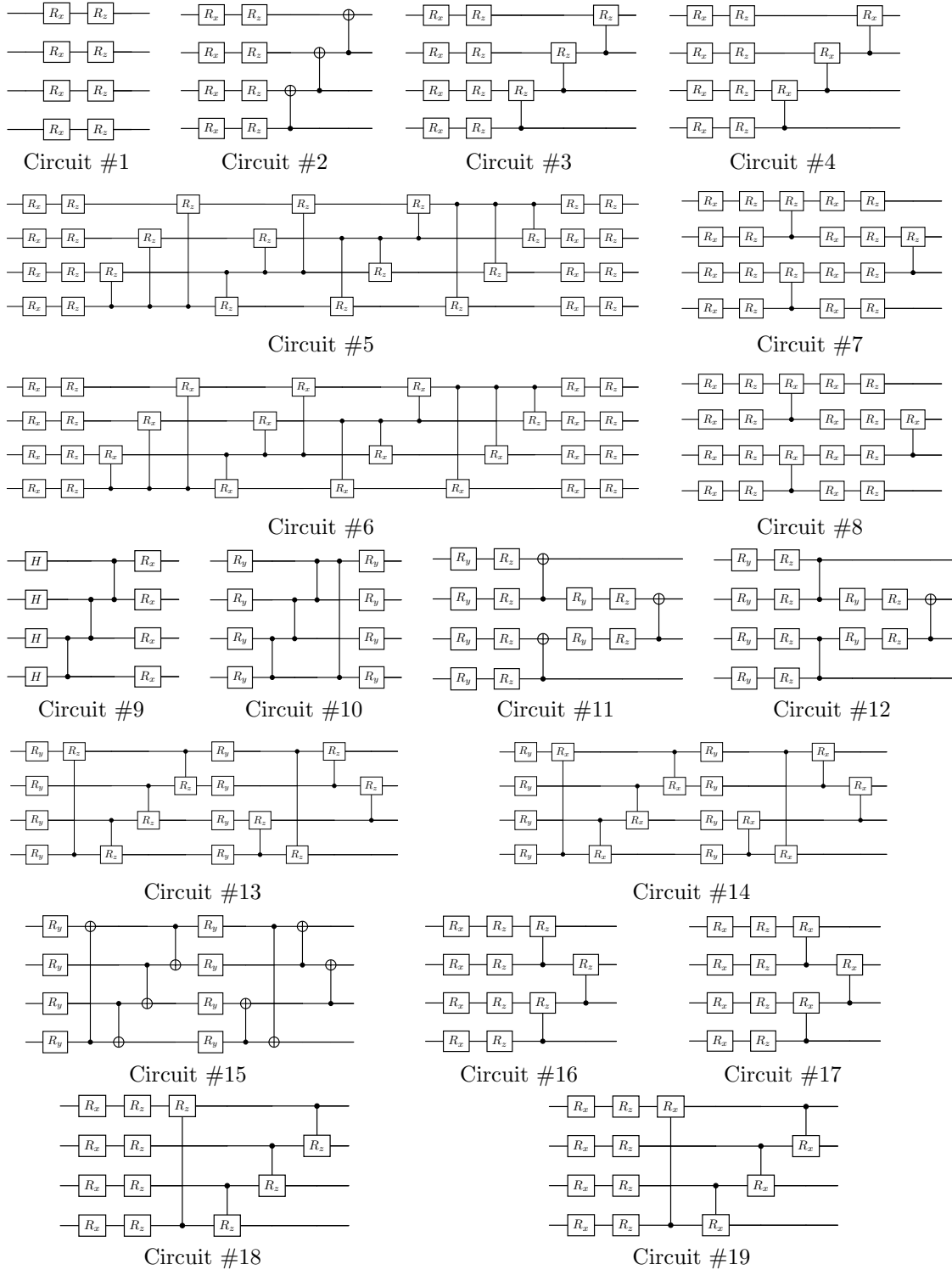


Figure S2: Ansatz Circuits #1 to #19 from [27]

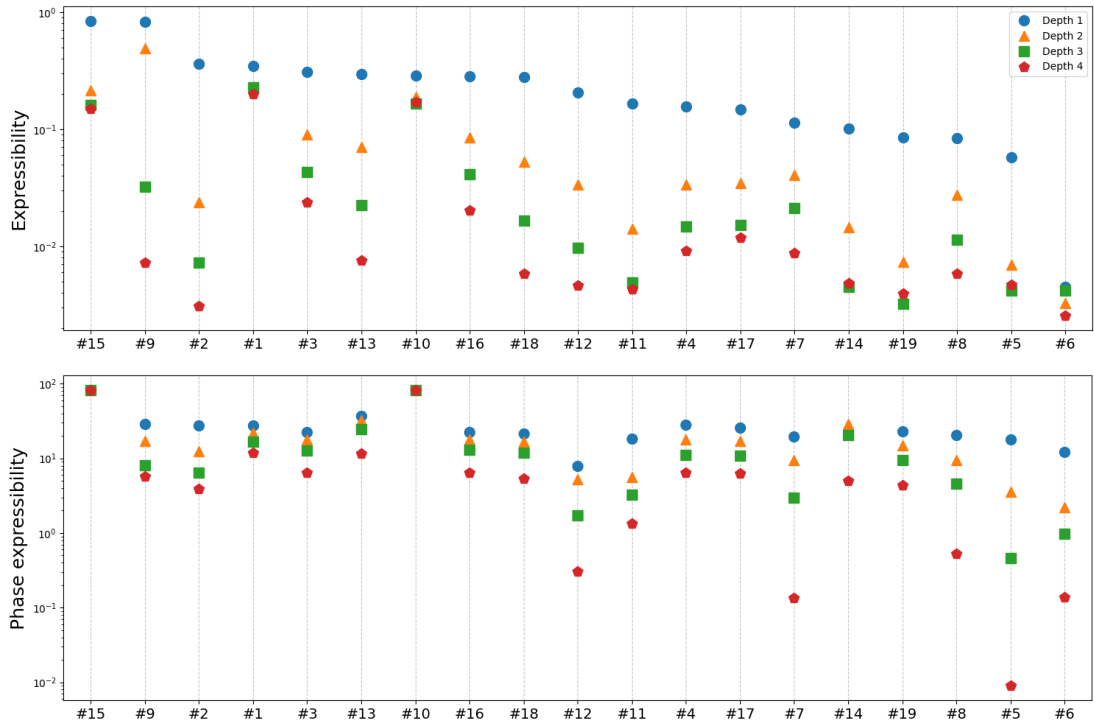


Figure S3: Expressibility and Phase Expressibility for ansatz circuits #1 to #19 with 4 qubits

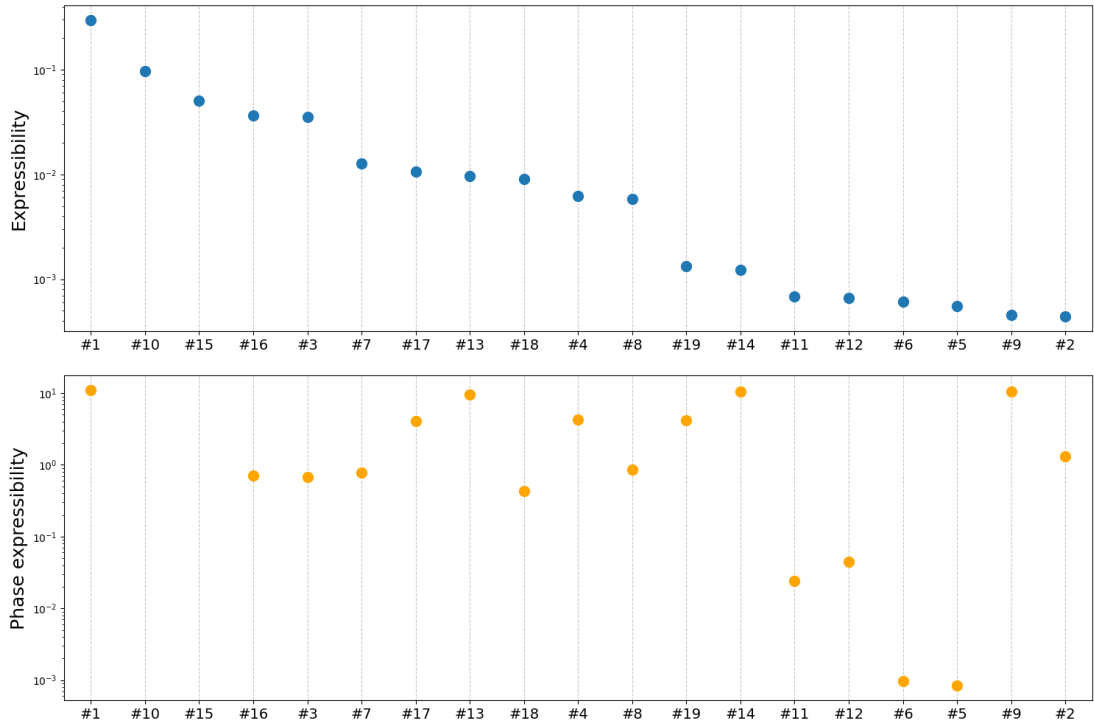
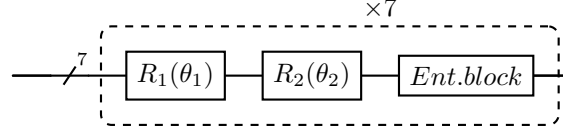
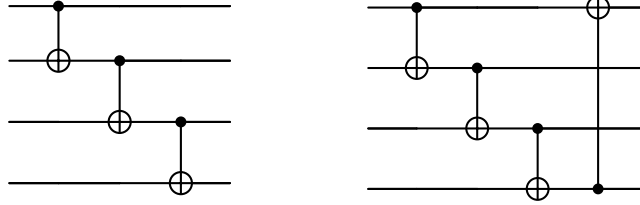


Figure S4: Expressibility and Phase Expressibility for ansatz circuits #1 to #19 with 7 qubits, 7 depths. The phase expressibility for #10 and #15 are omitted because they yield infinite values.



(a) Circuit templates for Table #3



(b) Linear entanglement type (c) Circular entanglement type

Figure S5: (a) Template circuit diagram for ansatz circuits #20 to #37; (b), (c) Illustration of the two entanglement types

Circuits	R_1	R_2	Ent. Gate	Ent. Type	Phase Expr.	Expr.
#20	R_z	R_y	C_x	Linear	1.52603	0.00047
#21	R_z	R_y	C_y	Linear	1.52767	0.00074
#22	R_z	R_y	C_z	Linear	0.42036	0.01252
#23	R_z	R_x	C_x	Linear	1.48493	0.00085
#24	R_z	R_x	C_y	Linear	0.95908	0.00088
#25	R_z	R_x	C_z	Linear	0.40457	0.01908
#26	R_x	R_y	C_x	Linear	0.51629	0.00048
#27	R_x	R_y	C_y	Linear	0.69513	0.00050
#28	R_x	R_y	C_z	Linear	0.99228	0.00109
#29	R_z	R_y	C_x	Circular	1.08200	0.00089
#30	R_z	R_y	C_y	Circular	0.85847	0.00065
#31	R_z	R_y	C_z	Circular	0.21520	0.00179
#32	R_z	R_x	C_x	Circular	0.88983	0.00060
#33	R_z	R_x	C_y	Circular	1.17551	0.00066
#34	R_z	R_x	C_z	Circular	0.22607	0.00244
#35	R_x	R_y	C_x	Circular	0.43104	0.00033
#36	R_x	R_y	C_y	Circular	0.54746	0.00092
#37	R_x	R_y	C_z	Circular	1.02731	0.00112

Figure S6: Expressibility and Phase Expressibility of the Ansatz Circuit with Structures Presented in Figure 8